Materials Science and Engineering A 527 (2010) 2738–2746

Contents lists available at ScienceDirect

Materials Science and Engineering A

journal homepage: www.elsevier.com/locate/msea

Orientation gradients and geometrically necessary dislocations in ultrafine grained dual-phase steels studied by 2D and 3D EBSD

Marion Calcagnotto*, Dirk Ponge, Eralp Demir, Dierk Raabe

Max-Planck-Institut für Eisenforschung, Max-Planck-Str. 1, 40237 Düsseldorf, Germany

ARTICLE INFO

Article history:
Received 1 July 2009
Received in revised form
22 December 2009
Accepted 6 January 2010

Keywords:
Dual-phase steel
Grain refinement
Orientation gradient
GND
3D EBSD

ABSTRACT

We study orientation gradients and geometrically necessary dislocations (GNDs) in two ultrafine grained dual-phase steels with different martensite particle size and volume fraction (24 vol.% and 38 vol.%). The steel with higher martensite fraction has a lower elastic limit, a higher yield strength and a higher tensile strength. These effects are attributed to the higher second phase fraction and the inhomogeneous transformation strain accommodation in ferrite. The latter assumption is analyzed using high-resolution electron backscatter diffraction (EBSD). We quantify orientation gradients, pattern quality and GND density variations at ferrite–ferrite and ferrite–martensite interfaces. Using 3D EBSD, additional information is obtained about the effect of grain volume and of martensite distribution on strain accommodation. Two methods are demonstrated to calculate the GND density from the EBSD data based on the kernel average misorientation measure and on the dislocation density tensor, respectively. The overall GND density is shown to increase with increasing total martensite fraction, decreasing grain volume, and increasing martensite fraction in the vicinity of ferrite.

1. Introduction

Dual-phase (DP) steels are low-carbon low-alloy materials with 20–30 vol.% martensite in a ductile ferrite matrix. As they combine high strength and good formability at low production costs they are widely used for automotive applications [1]. In response to the increasing demand for fuel efficiency and occupant safety, it was shown that grain refinement is an effective tool to strengthen dual-phase steels without raising alloying costs or allowing a decrease in ductility [2–5]. In this study, ultrafine grained DP steels with different martensite fractions were fabricated by large strain warm deformation of a plain C–Mn ferrite–pearlite steel and subsequent intercritical annealing.

Various studies aimed at a better understanding of the excellent mechanical properties of dual-phase steels [6–34]. There is broad consensus that the low elastic limit (defined as the first deviation from Hooke's law in the stress–strain curve), the continuous yielding and the high strain hardening rate are a consequence of the austenite-to-martensite transformation which involves a volume expansion. In our materials, the volume expansion is approximately 2.9% at the martensite start temperature.[1] The strains produced by the transformation result in residual stresses in the surrounding ferrite [6,7]. These internal stresses are assumed to facilitate plastic flow and hence, reduce the elastic limit. Furthermore, the volume change induces plastic deformation of adjacent ferrite grains and, therefore, creates a high density of unpinned dislocations in the vicinity of martensite [8–10] as was qualitatively studied by transmission electron microscopy (TEM) [11–13]. These dislocations are assumed to be (at least partly) mobile during the early stages of deformation and contribute to work hardening. The heterogeneous distribution of dislocations is supposed to control continuous yielding in dual-phase steels. It is assumed that the deformation starts in ferrite areas with low dislocation densities and spreads with increasing plastic strain into regions with higher dislocation densities [14].

At least a part of the adjacent ferrite grains has to deform plastically owing to the volume expansion during austenite-to-martensite transformation. During this deformation, geometrically necessary dislocations (GNDs) are required for maintaining lattice continuity [35–37] and statistically stored dislocations (SSDs) evolve from random trapping processes [36]. After such transformation-induced deformation, residual stresses remain due to the inhomogeneity of the plastic deformation throughout the

* Corresponding author. Tel.: +49 211 6792 416; fax: +49 211 6792 333.
E-mail addresses: m.calcagnotto@mpie.de (M. Calcagnotto), d.ponge@mpie.de (D. Ponge), e.demir@mpie.de (E. Demir), d.raabe@mpie.de (D. Raabe).

[1] The calculation of the volume expansion is based on the equilibrium chemical composition of austenite at the intercritical annealing temperature calculated using ThermoCalc, and the approximate equations for the martensite start temperature and for austenite-to-martensite volume expansion given in Refs. [23,24], respectively.

0921-5093/$ – see front matter © 2010 Elsevier B.V. All rights reserved.
doi:10.1016/j.msea.2010.01.004

grains [38]. Yet, it is still not understood to what extent geometrically necessary dislocations (GNDs), statistically stored dislocations (SSDs), and the associated residual stresses contribute to the yielding behavior of dual-phase steels. To address this question, a detailed quantification of the in-grain distribution of dislocations is necessary. However, corresponding findings presented to date are mainly based on coarse grained DP steels using theoretical calculations and TEM observations. While these works improved our understanding of local dislocation accumulation in the vicinity of ferrite–martensite interfaces, TEM investigations have the shortcoming that only a small area can be observed and that sample preparation can create defects or recovery of the microstructure. By means of high-resolution electron backscatter diffraction (HR-EBSD) it is possible to obtain information in a representative area even in ultrafine grained materials [39–41]. Individual crystallographic orientations as well as polarized arrays of dislocations with the same sign can be studied. By using automated orientation imaging microscopy (OIM), the electron beam scans the area inspected and records for each point the crystallographic orientation and a value for the quality of the Kikuchi pattern, viz. the Image Quality (IQ). The latter quantity is linked to lattice imperfections. Local changes in the lattice orientation reflect lattice curvature and can be used to calculate GND densities. In this study, two methods will be introduced to retrieve GND densities from the HR-EBSD data. In addition, we use 3D EBSD tomographic measurements to obtain information about the grain volume and about the true distribution of martensite in order to quantify their effects on GNDs. In contrast to TEM, EBSD does not depict individual dislocations and also, the angular and spatial resolution is lower. However, the resolution obtained here (around 0.3° and 50 nm, see below) is high enough to describe phenomena occurring on a tens of nm to μm scale.

2. Methods

2.1. Materials processing, metallography and mechanical testing

The investigated steel contains 0.17%C, 1.63%Mn, 0.28%Si, 0.036%Al, 0.0021%P, 0.0038%S and 0.0025%N (wt.%). The cast ingot was cut into samples of 50 mm × 40 mm × 60 mm. A 2.5 MN hot press was used for processing [42]. After 3 min austenitization, a one-step deformation pass was imposed for obtaining fully recrystallized austenite (Fig. 1). By controlled cooling, a ferrite–pearlite microstructure was obtained. For grain refinement to the μm-scale, large strain warm deformation was performed by exerting a four-step flat compression series (550 °C, total strain: 1.6). Subsequently, a heat treatment of 2 h at 550 °C was applied. The resulting microstructure was an ultrafine grained ferrite matrix with homogeneously distributed spheroidized cementite particles. Further processing and microstructure details are given in [43].

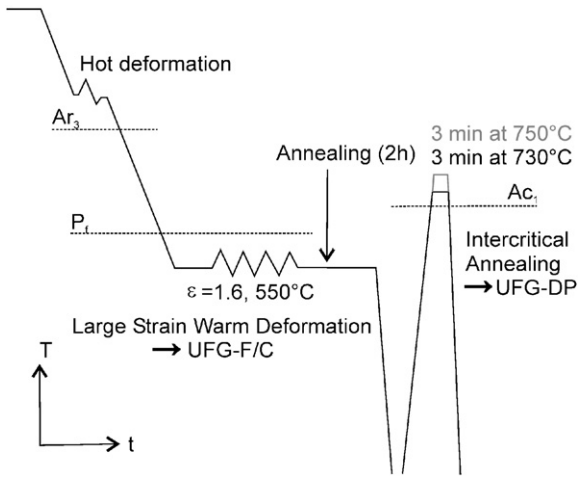

Fig. 1. Complete processing route for the production of ultrafine grained ferrite/martensite dual-phase steel (DP) from ultrafine grained ferrite/cementite (UFG-F/C) steel.

The final ferrite/martensite dual-phase structure was produced by short intercritical annealing in the ferrite/austenite region followed by quenching to transform all reversed austenite into martensite. The determination of the intercritical annealing parameters and their effect on the microstructure are described elsewhere [44,45]. Intercritical annealing was performed in a salt-bath furnace on samples of 12 mm × 10 mm × 75 mm. One sample (hereafter referred to as sample 730-DP) was held in the salt-bath at 730 °C for 3 min before it was water quenched to room temperature. For the second sample (750-DP) we used a temperature of 750 °C and the same holding time. With this procedure different martensite fractions were obtained in the two specimens to study the effects of the martensite particle size and of retained cementite on local orientation gradients. The phase fractions were determined on SEM micrographs. The ferrite grain size was investigated using the mean linear intercept method. Stress–strain curves were determined using flat tensile specimens with a cross-section of 3.5 mm × 5 mm and a gauge length of 10 mm (room temperature, constant cross-head speed with an initial strain rate of $0.5 \times 10^{-3}\ s^{-1}$).

2.2. Experimental setup for 2D EBSD

EBSD specimens were prepared by grinding, polishing, and electropolishing (Struers electrolyte A2; voltage: 30 V; flow rate 12 s^{-1}). EBSD maps were taken on a JEOL JSM 6500F electron microscope (SEM) equipped with field emission (FEG). The small beam diameter and its high brightness yield high-contrast Kikuchi patterns so that information about small orientation deviations even in areas with high dislocation densities like phase or grain boundaries was obtained. A high-speed DigiView CCD camera was used for pattern acquisition. Data were recorded at 50 nm step size and analyzed using the TSL software [46]. By choosing the highest possible image resolution for pattern processing and by optimizing the Hough transform parameters, an angular resolution of about 0.3° can be obtained [46,47]. The lateral resolution of the system is around 30 nm parallel to the tilt axis and around 90 nm perpendicular to the tilt axis, determined on iron at 15 kV [48]. Martensite was indexed as bcc ferrite and distinguished from ferrite by its significantly lower Image Quality and Confidence Index.

2.3. Experimental setup for 3D EBSD

For microstructure characterization in 3D we used automated serial sectioning via focused ion beam (FIB) combined with EBSD orientation microscopy in each section [49,50]. Our system consists of a Zeiss-Crossbeam XB 1540 FIB-SEM equipped with a Gemini-type FEG and an EDAX-TSL EBSD system. The ion beam column is mounted 54° from the vertical. The EBSD camera is placed on the opposite site. The sample is prepared by grinding and polishing of two perpendicular faces to produce a sharp rectangular edge. FIB milling (Ga^+ ions, accelerated at 30 kV) is performed on one surface starting from this edge. After milling, the sample is automatically shifted to the 70° EBSD position by tilting it 34° and adjusting the *y* position. EBSD is performed on the milled surface, before the sample is tilted back to the FIB position. For precise positioning between the steps, a marker is set. After each tilt, this marker is detected via image recognition. This software governs the beam shift which brings the sample to its reference position.

The step size and milling depth for the 3D maps was 100 nm. The scan size in each slice was 20 μm × 20 μm. The scan height is restricted by curtaining effects of the FIB milling which occur from

a certain distance below the top edge and deteriorates the EBSD pattern quality. To avoid shadow effects on the EBSD camera, additional surface areas had to be milled adjacent to the measured area. These areas were milled with 2 nA, as they do not require good surface finish. The fine milling of the scan area was conducted using a 500-pA beam. The total time for mapping 42 slices, including camera movement and image recognition, adds up to 23 h, which is within the long-term stability time of the instrument. The camera settings and the Hough parameters were set such that a pattern acquisition rate of 70 fps was obtained without significant decrease in pattern quality. Using these high-speed parameters the angular resolution is around 0.5°. A minor drawback of FIB milling DP steels is that very small amounts of retained metastable austenite may transform into martensite under the influence of the ion beam. However, the austenite distribution is not crucial for our analysis. Details about the 3D EBSD setup and its accuracy are given in [51–53]. Related studies on 3D reconstruction from EBSD data were presented in [54–58].

2.4. Calculating GND densities from EBSD data

Two approaches to calculating GND densities were applied and compared. The first one follows Kubin and Mortensen [59]. Based on the strain gradient model by Gao et al. [60], the authors define a GND array for simple cylinder torsion. Assuming a series of twist subgrain boundaries in the cylinder, each containing two perpendicular arrays of screw dislocations, the misorientation angle ϑ is related to the GND density ρ_{gnd},

$$\rho_{gnd} = \frac{2\vartheta}{ub}, \tag{1}$$

where u is the unit length and b is the magnitude of the Burgers vector. As a first order approach, the kernel average misorientation (KAM), which is retrieved directly from EBSD data, was chosen as a measure for the local misorientations. The KAM quantifies the average misorientation around a measurement point with respect to a defined set of nearest or nearest plus second-nearest neighbor points. Values above a predefined threshold (here it is 2°) are excluded from the calculation, because these points are assumed to belong to adjacent grains or subgrains (Fig. 2a).

The second method to evaluate GND densities is based on the calculation of the full dislocation density tensor as recently suggested in [61]. The components of that tensor α_{pi} are found using the neighbor-to-neighbor orientation gradients $g_{ij,k}$

$$\alpha_{pi} = e_{pkj} g_{ij,k} \tag{2}$$

where "e" indicates the permutation symbol. The orientation gradients are obtained from the EBSD orientation maps. First, the minimum misorientation between two adjacent points is calculated by applying the 24 crystal symmetry operators to both orientations. Then, the orientation gradient is calculated as the misorientation between the points divided by their distance. The orientation gradients are related to GNDs by use of a Frank's loop construction, Eq. (3). GNDs are characterized by the Burgers vector b (slip direction) and the tangent vector t (dislocation line direction). For simplicity, only the $\{1\,1\,0\}$ slip planes were used for the calculation [62,63]. Hence, there are 16 possible GND configurations in ferrite: 4 $\langle 1\,1\,1 \rangle$ edge dislocations and 4×3 $\langle 1\,1\,2 \rangle$ screw dislocations. As an ambiguity arises when relating 16 GND densities to nine dislocation tensor components, an energy minimization method was applied. Details of this approach are given in [61].

$$\alpha_{ij} = \sum_{a=1}^{9} \rho_{gnd}^{a} b_i^a t_j^a \tag{3}$$

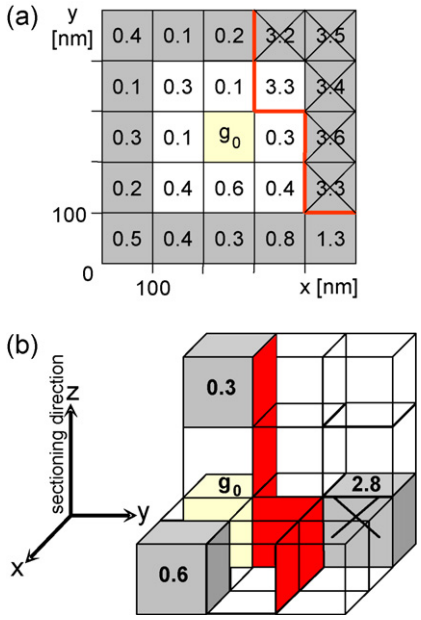

Fig. 2. Principles of the GND density calculation based on the kernel average misorientation (a) and the dislocation tensor (b) for the case of a 2nd neighbor evaluation and a step size of 100 nm. Grain boundaries are marked in red. Misorientations that exceed the minimum threshold value of 2° are excluded from the calculation of the average misorientation of neighboring points to a given measurement point g_0 and from the calculation of orientation gradients.

The calculation was done for each EBSD point and the orientation gradients were calculated with respect to its 2nd neighbors in 3D (Fig. 2b). If one of the three gradients exceeded the threshold angle of 2°, it was discarded and the GND density was calculated on the basis of the two other orientation gradients. For a physically meaningful GND density determination, the rank of the neighbor considered for the misorientation calculation is critical. The following points have to be considered when choosing the distance between two measurement points: (1) the distance has to be low enough to allow detailed information to be obtained; (2) the distance has to be high enough to average out scatter due to EBSD spatial resolution limits; and (3) to perform the calculations with misorientations above the angular EBSD resolution limits.

Fig. 3 shows a comparison of the two calculation methods (same EBSD data set) and the influence of the neighbor rank on the GND density calculation. The Image Quality (IQ) map shows the location of the grain boundaries and the martensite. In all maps, the misorientations along the grain boundaries and in the martensite exceed those in the ferrite grain interior. As the simple KAM values are not normalized by spacing, the KAM values increase with increasing neighbor rank. This is not the case for the calculated GND densities, as these values are distance normalized. Comparing the respective GND densities obtained for the 1st and 2nd neighbor sets reveals that the contrast between high and low GND density areas increases with increasing neighbor rank. Hence, from the 2nd neighbor GND maps, the location of grain boundaries and martensite can be more clearly distinguished. In the 1st neighbor sets the scatter is too high to yield distinct results. For this reason, a distance of 200 nm, which corresponds to the 2nd neighbor rank in the case of 3D EBSD measurements and to the 4th neighbor rank in the case of 2D EBSD measurements, was chosen for the GND calculations.

In general, both calculation methods yield very consistent results although the values obtained from the KAM-based calculation method tend to be a little lower. Moreover, this method

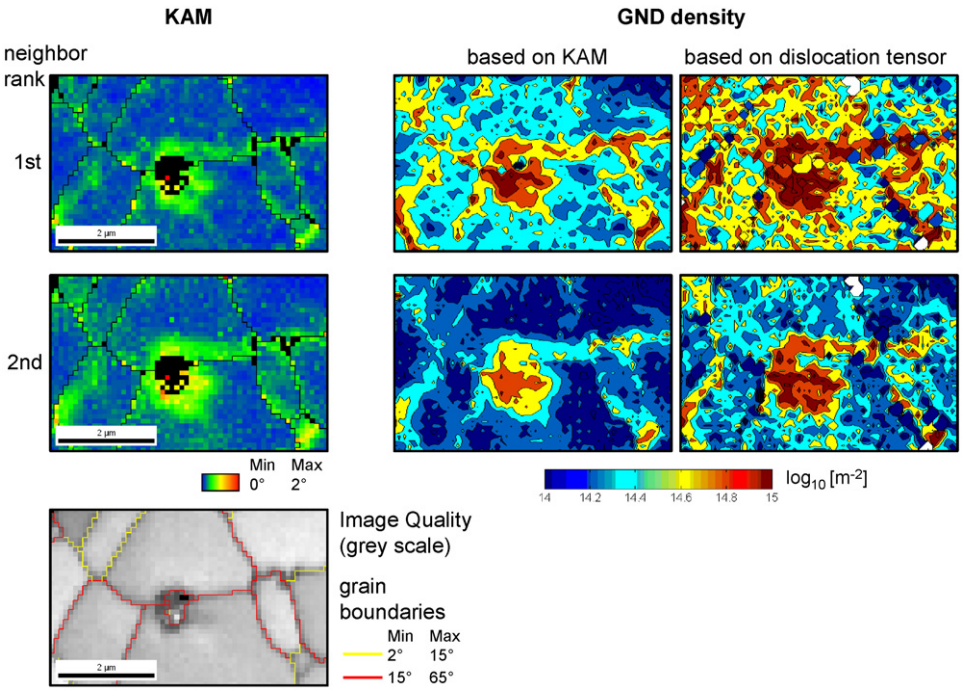

Fig. 3. The calculation of the GND densities based on the kernel average misorientation (KAM) and the dislocation tensor yield similar results. The 2nd neighbor rank, corresponding to a distance of 200 nm, is most suitable to obtain scatter-free information.

leads to a more even distribution of the GND densities. This can be attributed to the better statistics associated with the KAM-based method. Using the KAM, the local misorientation is calculated as an average of up to 16 values (in the 2nd neighbor configuration), whereas the maximum number of orientation gradients used for the formation of the dislocation tensor is 3 (Fig. 2). It can be concluded that both methods are appropriate to calculate GND densities from EBSD data sets.

It must be mentioned that the threshold value of 2° which is physically reasonable for ferrite does not apply for martensite. Due to the lattice distortion during martensite formation, misorientations above 2° can be present inside a single martensite variant. In fact, orientation gradients of up to 5° at a distance of 200 nm occurred frequently in our EBSD data. These misorientations were excluded from the calculations. Therefore, the GND density in the martensite might be slightly underestimated in our analysis. Moreover, the GND density distribution in martensite appears to be uniform, as most of the values considered for the calculation are slightly below 2°. However, the true GND density in martensite is not critical for the present investigation.

3. Results and discussion

3.1. Microstructure and mechanical properties

The initial ferrite/cementite (UFG-F/C) steel consists of an ultrafine grained ferrite matrix and finely dispersed spheroidized cementite particles distributed mostly along ferrite grain boundaries (Fig. 4a). Sample 730-DP is characterized by a ferrite matrix with 24 vol.% mostly isolated martensite particles and 2 vol.% cementite (Fig. 4b) The average ferrite grain size is 1.4 μm. Increasing the intercritical temperature to 750 °C leads to the complete dissolution of cementite and to an increase in the martensite fraction to 38 vol.% (Fig. 4c). The ferrite grain size decreases slightly to 1.2 μm due to progressive austenite grain growth.

Fig. 5 shows the engineering stress–strain curves of the two dual-phase steels. For comparison, the starting material (UFG-F/C) is included. The UFG-F/C steel exhibits the common features of this material, i.e. relatively high yield strength, pronounced Lüders straining and a low strain hardening rate. The replacement of cementite by martensite leads to a significantly lower yield ratio and to continuous yielding, whereas total elongation is decreased.

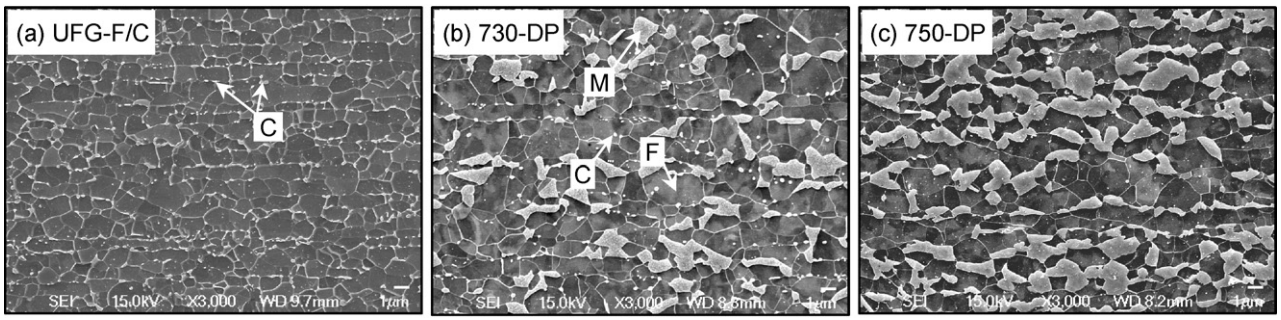

Fig. 4. SEM micrographs of the samples discussed in this study. (a) Ultrafine grained ferrite/cementite (UFG-F/C) steel obtained after large strain warm deformation. (b and c) Ferrite/martensite dual-phase structure obtained by subsequent intercritical annealing at 730 °C (730-DP, 24 vol.% martensite) and 750 °C (750-DP, 38 vol.% martensite), respectively. F: ferrite, M: martensite, C: cementite.

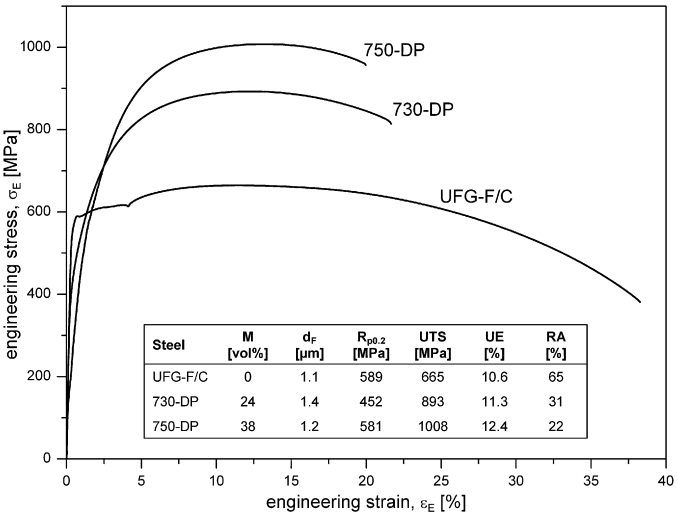

Steel	M [vol%]	d_F [μm]	$R_{p0.2}$ [MPa]	UTS [MPa]	UE [%]	RA [%]
UFG-F/C	0	1.1	589	665	10.6	65
730-DP	24	1.4	452	893	11.3	31
750-DP	38	1.2	581	1008	12.4	22

Fig. 5. Engineering stress–strain curves of the starting ultrafine grained ferrite/cementite steel (UFG-F/C) and the two dual-phase steels annealed at 730 °C (730-DP) and at 750 °C (750-DP) containing 24 vol.% and 38 vol.% martensite, respectively. M: martensite, d_F: average ferrite diameter, UTS: ultimate tensile strength, UE: uniform elongation, RA: reduction in area. Initial strain rate: 0.5×10^{-3} s^{-1}.

Increasing the martensite fraction leads to a lower elastic limit. This effect was explained in terms of residual stresses [21,31]. As the fraction of ferrite–martensite interfaces increases with increasing martensite fraction, a higher fraction of ferrite is affected by the martensitic phase transformation and hence, higher residual stresses are introduced into the matrix. This might be the reason why the elastic limit in ferrite is locally reached earlier during tensile deformation which is reflected by the lower initial slope of the curve with higher martensite fraction (750-DP). As both DP steels were stored at room temperature before tensile straining, dislocation locking by segregation of solute carbon does not occur, and the reoccurrence of a yield point is suppressed. The 750-DP sample has a tensile strength of 1003 MPa (table in Fig. 5) which is about 100 MPa above that of the 730-DP steel. The offset 0.2% offset yield strength ($R_{p0.2}$) is higher, too. The higher strength levels are generally attributed to the higher phase fraction of the hard second phase and can be approximated by a volumetric linear rule of mixtures [15,17]. The uniform elongation is hardly affected by the martensite fraction. Yet, as the plastic strain of the martensite phase is negligible, the total elongation to fracture is reduced with increasing martensite fraction. The initial strain hardening rate in both dual-phase steels is very high. This behavior is commonly interpreted in terms of local dislocation accumulation [18,30] introduced by the martensitic transformation.

The three curves show how strong the influence of martensite on plastic behavior of ferrite is and hence, how important it is to obtain quantitative information about the in-grain misorientations caused by the martensitic phase transformation.

3.2. Orientation gradients and GNDs in 2D

The enhanced dislocation density around martensite (athermal transformation) compared to cementite (diffusional transformation) can be visualized by using a high-resolution EBSD analysis placing emphasis on local orientation gradients at interfaces. Fig. 6 shows two such EBSD maps of sample 730-DP (a,c) and 750-DP (b,d). In these maps, the grey scale maps correspond to the Image Quality (IQ). The darker the color, the lower is the IQ value and the higher the lattice distortion. This measure allows one to distinguish the martensite clearly from the matrix as it exhibits higher lattice distortion. The color maps show the kernel average misorientation (KAM). Here, the average misorientation of an EBSD point is calculated with respect to all neighbors at 300 nm distance (values above 2° are excluded). As expected, the largest orientation gradients are found within the martensite islands. These KAM values are even underestimated due to the low threshold value of 2° (see discussion above). More importantly, the KAM maps reveal considerable orientation gradients spreading from the ferrite–martensite (FM) phase boundaries into the ferrite grain interior as was shown, yet not quantified, by the authors in a previous paper [64]. Each martensite particle is surrounded by at least one distinct orientation gradient in one of its neighboring ferrite grains, independent of the martensite particle size. One could expect that larger par-

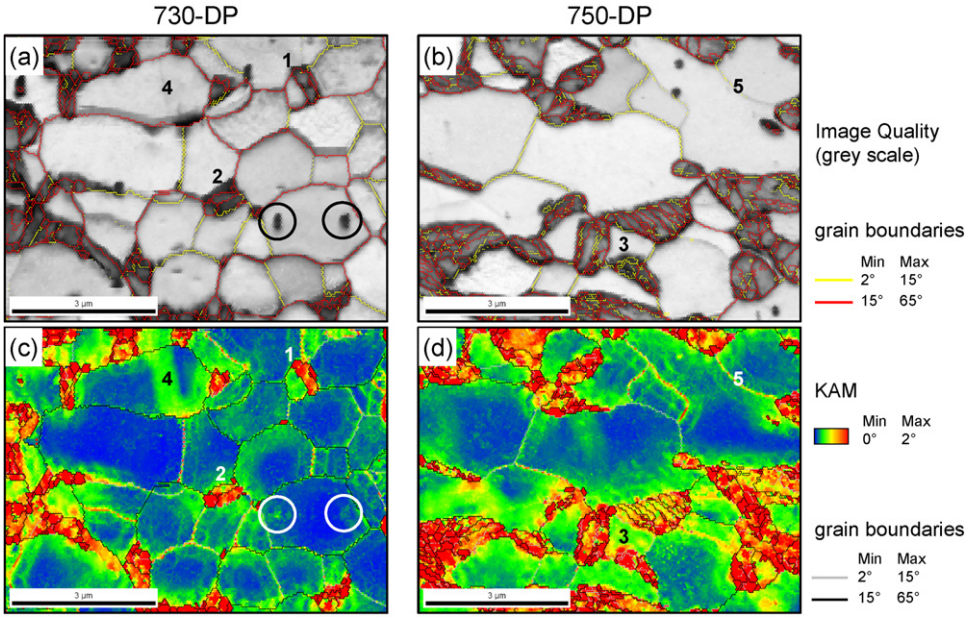

Fig. 6. Orientation gradients near ferrite–ferrite grain boundaries, ferrite–cementite phase boundaries and ferrite–martensite phase boundaries in the dual-phase (DP) steels containing 24 vol.% martensite (730-DP) and 38 vol.% martensite (750-DP). (a and b) Image Quality maps, where light values indicate high Image Quality, hence low lattice distortions. (c and d) Respective kernel average misorientation (KAM) maps. Distinctive features are numbered and described in the text.

ticles affect larger volume fractions of the adjacent ferrite grains, because the absolute volume increase is higher during transformation. However, even very small martensite particles cause strong local plastic deformation. A possible explanation is that smaller austenite particles have higher carbon content and, hence, undergo larger volume expansion [65]. Another aspect is the distribution of martensite around the ferrite grain. The more of the ferrite grain is surrounded by martensite, the higher the resulting in-grain orientation gradients. Cementite (encircled in Fig. 6) is not surrounded by notable orientation gradients. This confirms the experimental accuracy of the approach. The region affected by martensite is not necessarily distributed homogeneously around martensite particles, as can be seen when comparing the particles numbered (1) and (2). It is noteworthy, that orientation gradients are visible in ferrite grains of all sizes, even in very small ferrite grains with diameters of only 500–1000 nm. In case of a high number of martensite neighbors, these grains are sometimes entirely affected by the shape accommodation, i.e. the whole grain is work-hardened after martensitic phase transformation (grain number 3). There are also some minor dislocation accumulations visible at the ferrite–ferrite (FF) grain boundaries. Yet, the frequency of these gradients is scarce and less pronounced than at the FM interfaces. Furthermore, it is possible that the gradients arise from martensite particles present below or above the FF grain boundary (see 3D analysis below). Subboundaries with misorientation below 2° appear as regions of high misorientations (numbers 4 and 5) which must not be attributed to the martensitic phase transformation. The overall GND density in the ferrite was calculated on the basis of two HR-EBSD scans sized 10 μm × 20 μm. It is 1.9×10^{14} m^{-2} for the 730-DP and 2.4×10^{14} m^{-2} for the 750-DP. We see that the overall dislocation density in ferrite is increased with increasing martensite fraction, i.e. a higher ferrite fraction experiences local plastic deformation due to the martensitic phase transformation. The introduction of additional dislocations decreases the average spacing between dislocations, which is linked to the yield strength of the material [66]. The EBSD results thus provide an experimental explanation for the higher $R_{p0.2}$ yield strength of the 750-DP. Regarding the Hall-Petch relationship, another reason for the higher strength levels in the 750-DP might be the slightly smaller ferrite grain size (1.2 μm compared to 1.4 μm for the 730-DP). Beside the higher martensite fraction, another reason for the lower GND density in the 730-DP could be the presence of cementite which lowers the carbon content of austenite and thus reduces the transformation strain. Due to the low-alloy content, precipitations are unlikely to occur and therefore do not contribute to the strength increase.

In order to obtain more quantitative information about orientation gradients a number of misorientation profiles were retrieved from the texture maps at both the FF and FM interfaces. The starting point of each profile vector is the respective interface and the end point is the grain center. An example is shown in Fig. 7. The position of the two profile vectors is indicated in the KAM map. The misorientation profile shows the misorientation of a point with respect to the origin. The misorientation profiles do not depend on the overall martensite fraction. Therefore, this analysis includes both the 730-DP and the 750-DP. The FF curve shows a sudden step in the initial misorientation to a value of 0.5°, which can be attributed to lattice imperfections in the immediate vicinity of the FF grain boundaries. After this initial step there is no further increase and the misorientation values remain in the normal scatter range resulting from the spatial resolution of the EBSD system. The misorientation profile starting from the FM interface increases more gradually compared to the FF profile and reaches a much higher value of 1.4° at a distance of around 2 μm from the FM interface. In order to obtain a statistically more robust result, 20 misorientation profiles from different scans were analyzed for a set of different FF and FM interfaces. They all show the same tendencies described above. To obtain a simple yet clear measure for the local orientation gradients emanating from the two types of interfaces, the average misorientation at a distance of 1 μm was determined. It is in average 0.6° in front of FF grain boundaries and 1.2° in front of FM boundaries. The values are included in Fig. 7a (on the x-axis at 1 μm) together with the overall standard deviation for either case. For the FF interfaces the scatter is in the range of the angular resolution of the EBSD system (~0.3°). This indicates that the misorientation profiles reflect a pure grain boundary effect, which is consistently observed. In contrast, the scatter for the FM interfaces is larger. The main reason for this scatter is the inhomogeneity of the in-grain arrangement of the orientation gradients in the ferrite grains, i.e. shape accommodation due to the volume expansion during austenite-to-martensite transformation is realized inhomogeneously in the ferrite grains. Besides the angular resolution, another reason for the influence of the scatter in both profiles is the overall low values of the misorientations. In all cases, however, the orientation gradients emanating from FF boundaries are generally smaller by a factor of two when compared to those stemming from FM interfaces.

From the KAM values, the GND density was calculated (Fig. 7c). The values vary from about 2.5×10^{14} m^{-2} close to the martensite

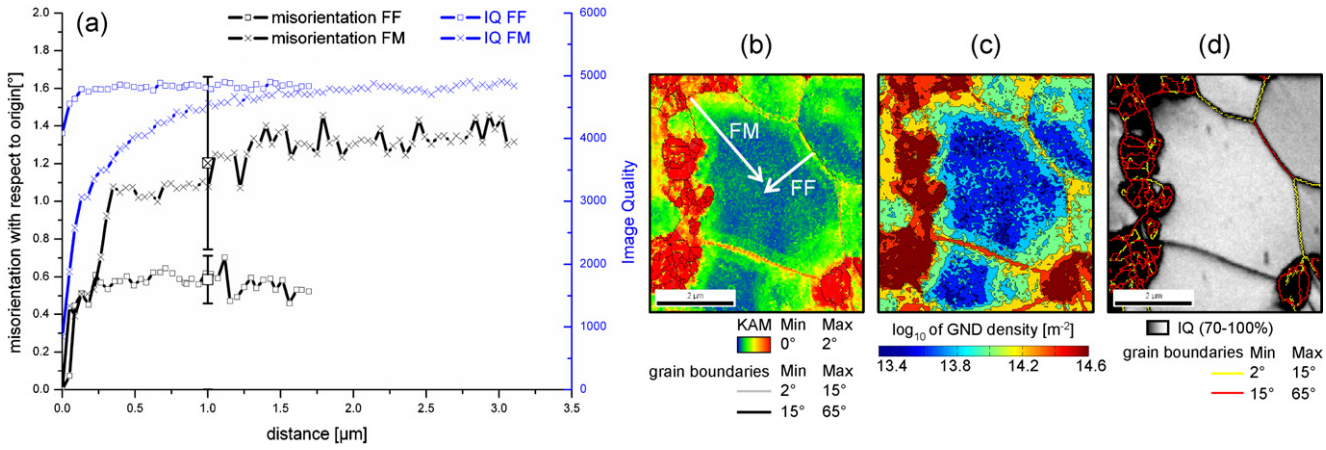

Fig. 7. (a) Misorientation and Image Quality (IQ) evolution from grain boundary to grain center obtained from 2D profile vectors starting from ferrite–martensite (FM) interfaces and ferrite–ferrite interfaces (FF) indicated in (b). Error bars show the statistical result obtained from a range of misorientation profiles. (b) Kernel average misorientation (KAM) map and grain boundaries. (c) GND density calculated from kernel data. (d) IQ map showing the gradual decrease of dislocations from the ferrite–martensite boundaries to the center.

particles to around 2.5×10^{13} m^{-2} in the grain interior. The boundary in the lower left part of the image is a subgrain boundary with a misorientation <2°, so that the GND density calculated in this area is extraordinarily high. The calculated GND densities coincide well with the data reported in the literature based on TEM [14,67] and on theoretical investigations [20]. The TEM studies [14,67] yield dislocation densities which are somewhat higher than the ones presented in this study. The reason is that statistically stored dislocations are additionally counted when evaluating TEM images.

As described above, the Image Quality of the diffraction patterns is also a suitable though qualitative indicator for the total defect density since it reflects the influence of both GNDs and SSDs on the distortion of the diffraction pattern. The in-grain change in the IQ value (Fig. 7d) is demonstrated exemplarily on the basis of the two profile vectors indicated in Fig. 7b. The IQ profile curves show the change in the IQ values with respect to the origin. They run nearly parallel to the respective misorientation profiles (Fig. 7a). The FF IQ profile shows a step close to the grain boundary before it becomes horizontal. In contrast, the FM IQ profile starts with a much lower IQ value and increases gradually up to maximum values in the interior of the ferrite grain. The sudden step of the IQ in the FF profile is due to the overlapping of the Kikuchi patterns along the grain boundary. In the FM IQ curve, this effect is clearly overlaid by the additional dislocations and plastic strains introduced by the martensitic phase transformation. As the pattern quality (IQ) is much more sensitive to surface preparation, surface roughness, contamination, chemical composition, and system calibration than the kernel average misorientation, the values obtained from it must be regarded as qualitative in nature and are hence not used for further calculations. Yet, as an additional evidence for the transformation-induced microstructure inhomogeneity inside the ferrite grains, the pattern quality measure deserves consideration.

In general, the orientation gradients emanating from both FF and FM boundaries are relatively small. However, they reveal important information about the distribution of lattice defects inside the ferrite. The misorientation and pattern quality profiles reveal that the ferrite grains abutting the FM interfaces experience larger values and wider regions of lattice distortion and an enhanced dislocation density than the corresponding areas in the vicinity of the FF grain boundaries.

3.3. Orientation gradients and GNDs in 3D

The 2D analysis revealed important information about the in-grain accommodation of transformation strains in ferrite grains. As a range of grains was analyzed in 2D, statistical errors are small and the findings are reliable. However, the true distribution of martensite and its effect on the GND distribution in the ferrite cannot be resolved by 2D sections alone. For example, an enhanced KAM value is expected all around the martensite particle. Hence, it is possible to observe high dislocation densities in ferrite in 2D sections, which arise from a martensite islands lying below or above this section. This effect is demonstrated in Fig. 8a where the IQ maps and respective KAM maps of two successive sections, separated by 100 nm, are shown. In the first section, considerable misorientations are detected in the center although no martensite is present (arrows). The next slice reveals that those misorientations stem from the martensite particle lying below the first section. The 3D cut along the indicated rectangle reveals the true distribution of the orientation gradients around the martensite (Fig. 8b). The 3D view demonstrates that the orientation gradients observed in 2D do not result from artifacts due to sample preparation. Furthermore, the previous observation from the 2D sections, that the GNDs are distributed inhomogeneously throughout the ferrite grains is found true also in the 3rd dimension (Fig. 8c).

By using a set of such 3D maps, information about grain volume characteristics can be obtained, namely, first, the effect of the ferrite grain volume on its average GND density and second, the effect of the martensite topology on the GND density in the ferrite. For this analysis, a set of complete ferrite grains was selected from the 3D EBSD data. In each slice, the grain size, the average KAM value, and the fraction of the interface covered by martensite were determined for each of the selected grains. This information was used to calculate grain volume, GND density, and the fraction of ferrite–martensite (FM) interfaces covering the grain. In total, 60 ferrite grains were analyzed in full 3D in this way. The number of evaluated large grains is limited due to the restricted total volume investigated (1680 μm^3). Furthermore, large grains containing subboundaries (see Fig. 6, number 4) or martensite particles in the grain interior were excluded from the statistics as these features pretend a higher GND density.

As a general trend, it was found that the average GND density in the ferrite decreases when the grain volume increases (Fig. 9). To understand this tendency, one has to consider that the interfaces (both FM and FF boundaries) enhance the nearby dislocation density, albeit to a different extent. The grain interior is supposed to have a low dislocation density as the material has undergone pronounced recovery during processing [43]. For this reason, the GND density (as well as the total dislocation density) increases with increasing ratio of boundary area to volume, hence, with decreas-

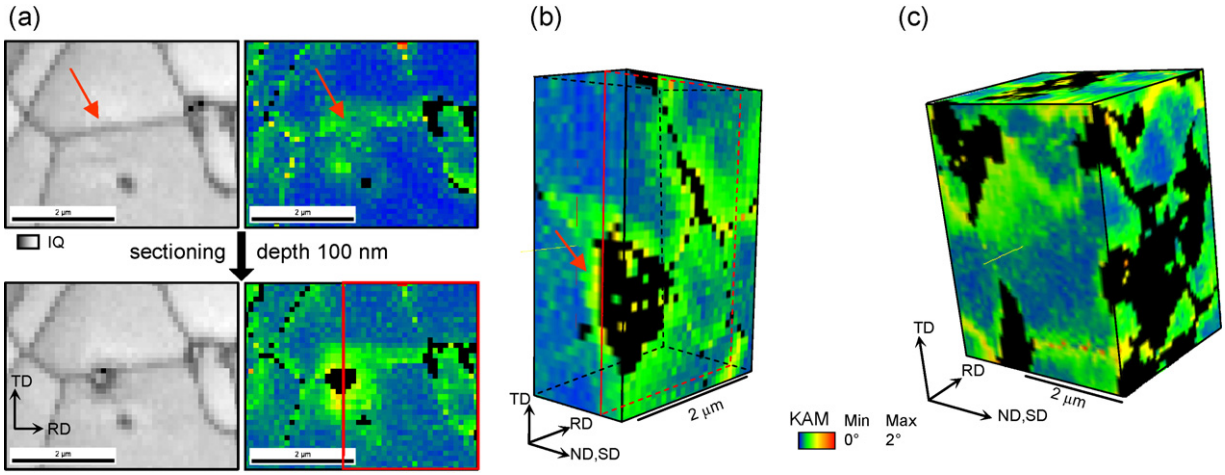

Fig. 8. (a) The Image Quality (IQ) and kernel average misorientation (KAM) maps (martensite is marked in black) of two successive slices reveal the enhancement of local misorientations in ferrite (arrows) due to martensite formation in three dimensions. The 3D view cut along the red rectangle illustrates this effect (b). 3D EBSD investigations in other areas further confirm that orientation gradients are distributed inhomogeneously throughout the ferrite grains (c). SD: sectioning direction.

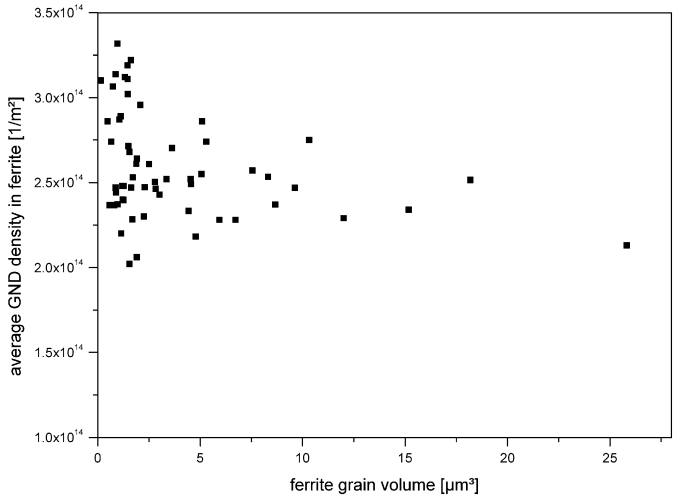

Fig. 9. Effect of grain volume on the average GND density in ferrite obtained from the 3D EBSD analysis. The data are taken from 60 ferrite grains. The overall decreasing tendency is overlaid by the effect of the fraction of ferrite–martensite interface which is resolved in Fig. 10.

ing grain size. Though meaningful, this diagram is incomplete as it does not account for the influence of the martensite distribution around a ferrite grain on the GND density. This is most evident when looking at the GND densities for small grains around 1 μm^3, where the scatter is remarkable. When correlating the GND densities with the respective interface fraction covered by martensite, it turns out that low GND densities correspond to grains with a low FM interface fraction and high GND densities to those with a high FM interface fraction.

For this reason, a second diagram was plotted to demonstrate this effect more clearly (Fig. 10). The grains were divided into classes of different grain sizes. Then, the average GND density of a grain is plotted as a function of the interface fraction covered by martensite. This diagram reveals that GND density is proportional to the FM interface fraction. In particular, smaller grains are more affected by a higher interface fraction of martensite (in terms of their average GND density) than larger grains. This is due to the fact that the volume affected by the martensitic phase transformation is restricted to areas adjacent to the phase boundary. This means that small grains can be entirely deformed when a high interface

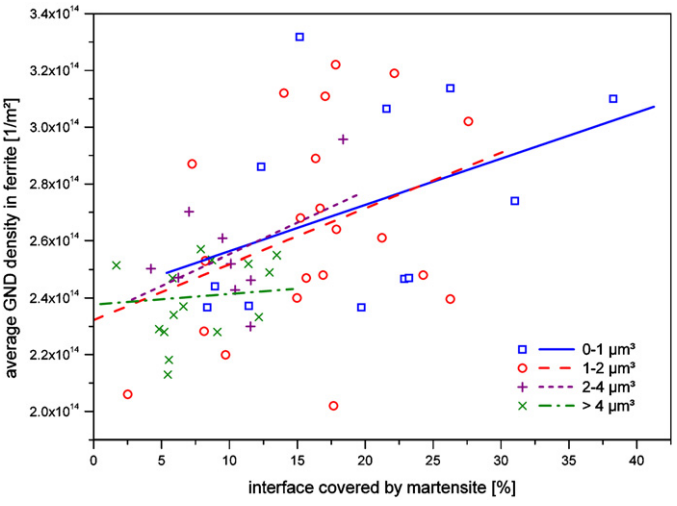

Fig. 10. The average GND density in a ferrite grain volume is proportional to the interface fraction covered by martensite. This effect is more pronounced for grain smaller than 4 μm^3. Data are taken from 60 ferrite grains based on 3D EBSD analysis.

fraction is covered by martensite (Fig. 6, number 3). In large grains, the effect of increasing FM interface fraction is less pronounced because the volume influenced by martensite is small compared to the total grain volume. This effect is only visible when comparing the lower three grain classes with the coarser grains. Thus, this grain size effect becomes relevant for grain volumes larger than 4 μm^3. The scatter of the data is quite high. This is explained by the inhomogeneous accommodation of the transformation strain in ferrite as was also revealed by the 2D EBSD scans. The scatter hence can be attributed to the different factors controlling local strain accommodation, namely ferrite grain size and orientation, as well as grain size and phase distribution of the surrounding grains.

4. Conclusions

Two ultrafine grained dual-phase steels with different martensite fractions were produced by large strain warm deformation and subsequent intercritical annealing. The effect of the volume expansion during martensitic phase transformation on orientation gradients and GNDs in ferrite was analyzed using high-resolution EBSD in 2D and 3D. The main conclusions are

- Orientation gradients originating from ferrite–martensite interfaces are distinctly higher than those initiated at ferrite–ferrite interfaces. The average misorientation at a distance of 1 μm from the boundary was 1.2° for ferrite–martensite interfaces, and 0.6° for ferrite–ferrite grain boundaries.
- Orientation gradients are generally present around each martensite particle, irrespective of particle size. The accommodation of transformation strain is realized inhomogeneously within the ferrite grains.
- The average GND density in the steel with 24 vol.% martensite is $1.9 \times 10^{14}\ m^{-2}$ compared to $2.4 \times 10^{14}\ m^{-2}$ for the steel containing 38 vol.% martensite. The higher fraction of immobile dislocations might contribute to the higher $R_{p0.2}$ yield strength of the latter steel. The enhanced dislocation density around martensite particles was verified by evaluating the Image Quality maps.
- The average GND density of a ferrite grain is proportional to the ferrite–martensite interface fraction surrounding it. This effect is most pronounced for ferrite grain volumes below 4 μm^3. In case of a high number of martensite neighbors, very small grains <1 μm^3 can be entirely work-hardened due to the martensitic phase transformation.
- High-resolution 2D and 3D EBSD is an appropriate tool to obtain information about the local distribution of dislocations in dual-phase steels. The GND density can be calculated both on the basis of the kernel average misorientation and on the dislocation tensor.

References

[1] K. Hulka, Mater. Sci. Forum 414–415 (2003) 101–110.
[2] P.H. Chang, A.G. Preban, Acta Metall. 33 (1985) 897–903.
[3] Z. Jiang, Z. Guan, J. Lian, Mater. Sci. Eng. A 190 (1995) 55–64.
[4] P. Tsipouridis, E. Werner, C. Krempaszky, E. Tragl, Steel Res. Int. 77 (2006) 654–667.
[5] K. Mukherjee, S. Hazra, P. Petkov, M. Militzer, Mater. Manuf. Process 22 (2007) 511–515.
[6] T. Sakaki, K. Sugimoto, T. Fukuzato, Acta Metall. 31 (1983) 1737–1746.
[7] Q. Chen, R. Kaspar, O. Pawelski, Z. Metallkd. 76 (1985) 348–352.
[8] R.G. Davies, Metall. Trans. A 10 (1979) 1549–1555.
[9] M.S. Rashid, in: A.T. Davenport (Ed.), Formable HSLA and Dual-phase Steels, The Metallurgical Society of AIME, New York, 1979, pp. 1–24.
[10] J.M. Rigsbee, J.K. Abraham, A.T. Davenport, J.E. Franklin, J.W. Pickens, in: R.A. Kot, J.W. Morris (Eds.), Structure and Properties of Dual-phase Steels, The Metallurgical Society of AIME, New York, 1979, pp. 304–329.
[11] D.K. Matlock, G. Krauss, L.F. Ramos, G.S. Huppi, in: R.A. Kot, J.W. Morris (Eds.), Structure and Properties of Dual-phase Steels, The Metallurgical Society of AIME, New York, 1979, pp. 62–90.

[12] A.M. Sherman, R.G. Davies, W.T. Donlon, in: R.A. Kot, B.L. Bramfitt (Eds.), Fundamentals of Dual-phase Steels, The Metallurgical Society of AIME, New York, 1981, pp. 85–94.
[13] D.A. Korzekwa, D.K. Matlock, G. Krauss, Metall. Trans. A 15 (1984) 1221–1228.
[14] A.M. Sarosiek, W.S. Owen, Mater. Sci. Eng. 66 (1984) 13–34.
[15] R.G. Davies, in: A.T. Davenport (Ed.), Formable HSLA and Dual-phase Steels, The Metallurgical Society of AIME, New York, 1979, pp. 25–39.
[16] G.R. Speich, R.L. Miller, in: R.A. Kot, J.W. Morris (Eds.), Structure and Properties of Dual-phase Steels, The Metallurgical Society of AIME, New York, 1979, pp. 145–182.
[17] J.Y. Koo, M.J. Young, G. Thomas, Metall. Trans. A 11 (1980) 852–854.
[18] N.K. Balliger, T. Gladman, Met. Sci. 15 (1981) 95–108.
[19] A. Rizk, D.L. Bourell, Scripta Metall. 16 (1982) 1321–1324.
[20] D.L. Bourell, A. Rizk, Acta Metall. 31 (1983) 609–617.
[21] R. Priestner, C.L. Aw, Scripta Metall. 18 (1984) 133–136.
[22] H.P. Shen, T.C. Lei, J.Z. Liu, Mater. Sci. Technol. 2 (1986) 28–33.
[23] M.S. Nagorka, G. Krauss, D.K. Matlock, Mater. Sci. Eng. 94 (1987) 183–193.
[24] Y.L. Su, J. Gurland, Mater. Sci. Eng. 95 (1987) 151–165.
[25] A.K. Jena, M.C. Chaturvedi, Mater. Sci. Eng. 100 (1988) 1–6.
[26] B. Grushko, B.Z. Weiss, Scripta Metall. 23 (1989) 865–870.
[27] A. Bhattacharyya, T. Sakaki, G.J. Wenig, Metall. Trans. A 24 (1993) 301–314.
[28] M. Sarwar, R. Priestner, J. Mater. Sci. 31 (1996) 2091–2095.
[29] A. Bag, K.K. Ray, E.S. Dwarakadasa, Metall. Mater. Trans. A 30 (1999) 1193–1202.
[30] W. Bleck, A. Frehn, J. Ohlert, Proceedings of the International Symposium on Niobium Niobium Science and Technology, Orlando, USA, 2001, pp. 727–752.
[31] U. Liedl, S. Traint, E.A. Werner, Comput. Mater. Sci. 25 (2002) 122–128.
[32] F.M. Al-Abbasi, J.A. Nemes, Int. J. Mech. Sci. 45 (2003) 1449–1465.
[33] C.Y. Kung, J.J. Rayment, Metall. Trans. A 13 (1982) 328–331.
[34] C.L. Magee, R.G. Davies, Acta Metall. 20 (1972) 1031–1043.
[35] J.F. Nye, Acta Metall. 1 (1953) 153–162.
[36] M.F. Ashby, Philos. Mag. 21 (1970) 399–424.
[37] E. Kröner, Int. J. Eng. Sci. 1 (1963) 261–278.
[38] G.E. Dieter, Mechanical Metallurgy, third ed., McGraw-Hill, New York, 1986.
[39] B.L. Adams, S.I. Wright, K. Kunze, Met. Trans. A 24 (1993) 819–831.
[40] A.J. Schwartz, M. Kumar, B.L. Adams (Eds.), Electron Backscatter Diffraction in Materials Science, Kluwer Acad/Plenum Publishers, New York, 2000.
[41] F.J. Humphreys, J. Mater. Sci. 36 (2001) 3833–3854.
[42] R. Kaspar, O. Pawelski, Materialprüfung 31 (1989) 14–16.
[43] R. Song, D. Ponge, D. Raabe, R. Kaspar, Acta Mater. 53 (2005) 845–858.
[44] M. Calcagnotto, D. Ponge, D. Raabe, ISIJ Int. 48 (2008), 1096-1011.
[45] M. Calcagnotto, D. Ponge, D. Raabe, Proceedings of the MS&T Conference and Exhibition, Pittsburgh, USA, 2008, CD-Rom.
[46] D. Dingley, J. Microsc. 213 (2004) 214–224.
[47] P.S. Bate, R.D. Knutsen, I. Brough, F.J. Humphreys, J. Microsc. 220 (2005) 36–46.
[48] S. Zaefferer, Ultramicroscopy 107 (2007) 254–266.
[49] J. Konrad, S. Zaefferer, D. Raabe, Acta Mater. 54 (2006) 1369–1380.
[50] N. Zaafarani, D. Raabe, R.N. Singh, F. Roters, S. Zaefferer, Acta Mater. 54 (2006) 1863–1876.
[51] S. Zaefferer, S.I. Wright, D. Raabe, Metall. Mater. Trans. A 39 (2008) 374–389.
[52] A. Bastos, S. Zaefferer, D. Raabe, J. Microsc. 230 (2008) 487–498.
[53] A. Khorashadizadeh, M. Winning, D. Raabe, Mater. Sci. Forum 584–586 (2008) 434–439.
[54] S.B. Lee, A.D. Rollett, G.S. Rohrer, Mater. Sci. Forum 558–559 (2007) 915–920.
[55] A.D. Rollett, S.B. Lee, R. Campman, G.S. Rohrer, Ann. Rev. Mater. Res. 37 (2007) 627–658.
[56] W. Xu, M. Ferry, F.J. Humphreys, Scripta Mater. 60 (2009) 862–865.
[57] W. Xu, M. Ferry, J.M. Cairney, F.J. Humphreys, Acta Mater. 55 (2007) 5157–5167.
[58] W. Xu, M. Ferry, N. Mateescu, J.M. Cairney, F.J. Humphreys, Mater. Charact. 58 (2007) 961–967.
[59] L.P. Kubin, A. Mortensen, Scripta Mater. 48 (2003) 119–125.
[60] H. Gao, Y. Huang, W.D. Nix, J.W. Hutchinson, J. Mech. Phys. Solids 47 (1999) 1239–1263.
[61] E. Demir, D. Raabe, N. Zaafarani, S. Zaefferer, Acta Mater. 57 (2009) 559–569.
[62] D. Raabe, Phys. Stat. Sol. A 149 (1995) 575–581.
[63] D. Raabe, Mater. Sci. Eng. A 197 (1995) 31–37.
[64] M. Calcagnotto, D. Ponge, D. Raabe, Proceedings of the 3rd Internatonal Conference on Thermomechanical Processing of Steels, Padova, Italy, 2008, CD-Rom.
[65] J.M. Moyer, G.S. Ansell, Metall. Trans. A 6 (1975) 1785–1791.
[66] U.F. Kocks, Philos. Mag. 13 (1966) 541–566.
[67] X.L. Cai, J. Feng, W.S. Owen, Metall. Trans. A 16 (1985) 1405–1415.